Topological enhancement of exciton-polariton coherence with non-Hermitian morphing

Ruiqi Bao [1],[*] Huawen Xu, Wouter Verstraelen, and Timothy C. H. Liew [†]

Division of Physics and Applied Physics, School of Physical and Mathematical Sciences, Nanyang Technological University,
Singapore 637371, Singapore

The non-Hermitian skin effect (NHSE) has been intensely investigated over the past few years and has unveiled new topological phases, which have no counterparts in Hermitian systems. Here we consider the hybridization between the NHSE in an exciton-polariton waveguide and a localized defect mode. By tuning the non-Hermiticity, we find that the resulting ground state of the system is both spatially extended and energetically separated from other modes in the system. When polariton lasing occurs in the system, we find an enhanced spatial coherence (of typically 30 times longer) compared to regular waveguides, which is robust in the presence of disorder.

I. INTRODUCTION

Coherence—the potential to display interference—is at the very heart of photonics. It corresponds to the presence of phase correlations, marking the ability of many bosons to act collectively. Photonic applications typically use coherence as the key feature setting them apart from electronic and other systems [1]. Arguably, the most important milestone in photonics was the invention of the laser, which uses stimulated boson scattering as a source of coherence [2].

Following progress in establishing coherence in the realization of atomic Bose-Einstein condensates [3], there has been an increased interest in the study of coherence in spatially extended optical systems such as (arrays of) vertical cavity surface emitting lasers [4] or the condensation of photons in microcavities [5] or waveguides [6], excitons [7], or exciton polaritons [8], which are considered their nonequilibrium counterpart [9]. It is clear, however, that the spatial coherence in these systems is still limited. Ideally, on chip devices typically seek a two-dimensional geometry (or less). However, for these dimensions long-range spatial coherence is impossible in uniform equilibrium systems [10]: a consequence of the ground state not being gapped and therefore not robust to fluctuations. The nonequilibrium nature of optical systems introduces additional fluctuations, which may deteriorate the spatial coherence further [11,12].

The advancement of fabrication techniques has allowed the engineering of a variety of arrays of lasing or cavity systems and such photonic crystals can mimic the behavior of electronic lattices. Inspired by electronic topological insulators this has given rise to the field of topological photonics. The field began with a photonic analogy of the quantum Hall effect [13–16], followed by the demonstration of a variety of other topological phases such as antichiral edge states [17,18], Su-Schrieffer-Heeger edge states [19,20], valley Hall effects [21,22], and higher-order topological insulators (corner modes) [23–27]. Most recently, it has been appreciated that the ubiquitous gain and loss processes throughout photonics allow for various non-Hermitian topological phases [28–33]. Among them, the non-Hermitian skin effect (NHSE) where all eigenstates are localized at the edge has drawn particular attention due to the breakdown of the celebrated bulk-edge correspondence [34]. A topological invariant known as the winding number is used to characterize the nontrivial topology in this case [35,36]. Furthermore, it has been proposed that combining systems with different topologies allows for morphed states [37,38]. While a satisfying amount of fundamental non-Hermitian physics has been uncovered, actual uses of non-Hermitian topology are seldom discussed. Here, we propose that the morphing of non-Hermitian topological states can enhance the spatial coherence length of photonic systems. We focus on the system of exciton-polaritons in planar microcavities, where spatial coherence is possibly most challenging to achieve given the two-dimensional nature of the system, nonequilibrium fluctuations, unavoidable disorder, and the presence of nonlinear interactions.

Exciton-polaritons are hybrid particles formed from cavity photons and quantum well excitons [8,39]. Excitons relaxing from higher energy states (possibly electrically injected) provide a gain mechanism for polaritons, while photons constantly leak out providing a loss mechanism. This non-Hermitian system supports the formation of a partially coherent state when the gain overcomes the loss. As polaritons are bosons, this is often considered as a nonequilibrium version of Bose-Einstein condensation. The light emitted shows a level of coherence such that the system is also identified as a form of laser or polariton laser. Unlike a regular laser, polariton lasers do not rely on population inversion and thus they can operate with lower threshold powers. However, their coherence is complicated by the presence of nonlinear interactions (due to interactions between excitons). The highest coherence of polariton lasers requires isolating the lasing mode in energy, which has been achieved in structures etched

_____

[*]ruiqi002@e.ntu.edu.sg
[†]timothyliew@ntu.edu.sg

so as to trap polaritons in all three dimensions [40]. While this technique is good for enhancing temporal coherence [41], the trapping of the condensate necessarily limits spatial coherence to the trap size. In spatially extended systems, it is common for multiple condensates to appear within an energy bandwidth. While spectrally resolving each mode shows a good spatial coherence of each mode [42], an ideal polariton laser would show spatial coherence without such spectral filtering. It is also understood that disorder limits the range of spatial coherence in spatially extended systems [43].

The same etching techniques to trap polaritons can be used to realize lattices for polaritons. This has supported the field of topological polaritons [44–52], where the typical objective is to engineer a band structure such that it isolates a small number of states in a band gap using topology to ensure robustness against structural variations and disorder. Being non-Hermitian systems, polaritons also support a variety of non-Hermitian topological effects, including exceptional points [53–55], bound-statein-continuum modes [56], NHSE [57–60], non-Hermitian corner modes [61], and end-mode lasing [62].

Here, we consider the hybridization of a polariton waveguide supporting non-Hermitian skin modes with the modes of an intentional defect (trap). The aim is to morph the ideal properties of the defect, namely the presence of a ground state well isolated in energy, with the ideal properties of the skin effect, namely the spreading of its wave functions over a controllable localization length. We find theoretically that the system can undergo polariton lasing in the ground state. This allows us to predict an enhanced spatial coherence length compared to that of a regular polariton waveguide. As is expected of most topological systems, we also find robustness of the attained spatial coherence in the presence of disorder. Finally, we show that the mechanism is still feasible in the presence of realistic levels of nonlinear interaction.

II. MODEL

It was pointed out in [58] that the NHSE can be attained in polariton systems by arranging a phase dependent coupling between two chains of modes with different gain/loss. Examples of realizing such a model include using the coupling between spin states in chains of elliptical micropillars [57], the coupling between vortex modes in chains of polariton rings [59], and most recently the coupling of spin states using Rashba-Dresselhaus spin-orbit coupling (RDSOC) [63,64] in liquid crystal filled microcavities [65]. The latter proposal has pointed out that the NHSE can occur in continuous waveguides, without a lattice. While our results should not depend on the precise underlying mechanism of the NHSE, the latter proposal will serve best our purpose given that spatial coherence was previously considered in similar one-dimensional waveguide [43,66] geometries and it will avoid modulation of the spatial coherence function by the presence of a lattice. Within such a model, the evolution of polaritons is described by

$$ i\hbar \frac{\partial \Psi_\pm}{\partial t} = \left(-\frac{\hbar^2 \nabla^2}{2m} + V \mp 2i\alpha \frac{\partial}{\partial x} - i\gamma_\pm \right) \Psi_\pm + \Delta_T \Psi_\mp. $$

(1)

Here $\Psi_\pm$ is the wave function of polaritons with $\pm$ spin (corresponding to the circular polarization of emitted light). m is the effective mass, V is a two-dimensional spatial potential profile of our considered microcavity, which is deeper inside the waveguide region [-20 meV; gray area as shown in Fig. 1(a)], α is the strength of RDSOC, Δ_T is the X-Y splitting existing in the microcavity, and $\gamma_\pm$ correspond to the decay rates of spin up and down polaritons.

It is instructive to first consider the system in a Hermitian regime, neglecting the loss term ($\gamma_\pm = 0$), which gives the dispersion shown in Fig. 1(b). The color bar used in the figure is calculated according to the degree of circular polarization S_z, which is defined as

$$ S_z = \frac{|\Psi_+|^2 - |\Psi_-|^2}{|\Psi_+|^2 + |\Psi_-|^2}. $$

(2)

In this situation, time-reversal symmetry is preserved; however, opposite spins propagate in opposite directions in a topological spin Hall effect (see the Appendixes).

Typically in a polariton system, the spin up and spin down decay rates would be the same. However, this changes if we apply a circularly polarized nonresonant pump, which serves as gain. We consider a spin up polarized, spatially uniform incoherent pump, resulting effectively in $\gamma_+ < \gamma_-$. We calculate the eigenstates' spatial distribution and find that, different from the Hermitian case [Fig. 1(d)], all eigenstates are localized at the right end of the waveguide as shown in Fig. 1(e). Introducing a spin down polarized pump would reverse this localization. This phenomenon known as the NHSE has no counterpart in Hermitian systems. To prove its topological nature, we calculate the complex energy spectrum under both a periodic boundary condition (PBC) and open boundary condition (OBC) as shown in Fig. 1(c). We find that the complex energy spectrum from the PBC forms a closed loop, which is a signature behavior of the NHSE [67]. In the NHSE, it is expected that all injected polaritons propagate along the same direction (right in this case; see the Appendixes).

III. MORPHING OF THE DEFECT MODE

Here, we consider the interplay between the NHSE and a trivial defect ground state (lowest real energy state). The defect state is governed by a region with deeper potential than the rest of the waveguide. This could be realized by coupling a micropillar to the waveguide or engineering a region with stronger light-matter coupling [41].

Given that the defect has a deeper potential, the ground state of the system could be expected to be localized in the defect. When $\delta\gamma = 0$ ($\delta\gamma = \gamma_+ - \gamma_-$) as the case without NHSE, the ground state's spatial profile is shown in Fig. 2(b). The spatial profile of this state changes drastically if we increase $\delta\gamma$. When $\delta\gamma$ is not sufficiently large, the mode will be slightly pulled into the waveguide area as shown in Fig. 2(c). Upon further increasing the decay difference, we find the mode extends within the whole waveguide at the right of the defect [Fig. 2(d)]. Eventually, with a larger $\delta\gamma$, the mode becomes localized at the right end, similar to other modes within the waveguide [Fig. 2(e)]. This effect occurs due to the competition between defect's trapping and localization of the NHSE. The localization length of the NHSE depends on
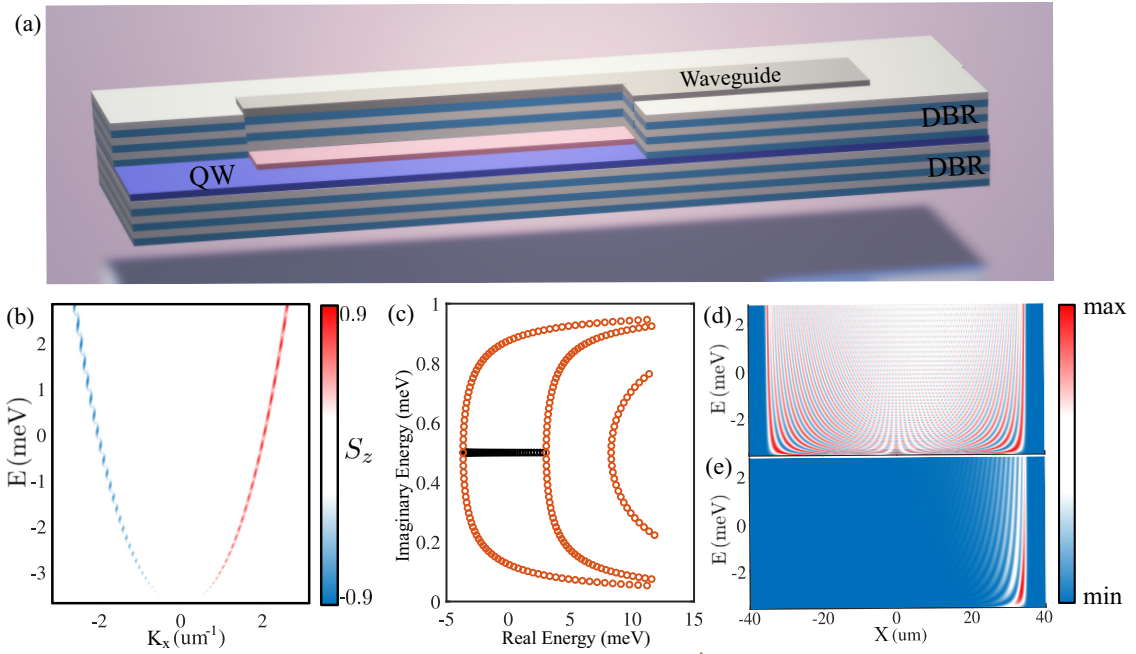
FIG. 1. (a) Schematic figure of a microcavity with an etched waveguide. The microcavity is formed by two sets of distributed Bragg reflectors (DBRs) sandwiching a quantum well (QW). (b) Calculated band structure with the consideration of RDSOC, where S_z represents the circular polarization. (c) Complex energy spectra calculated under different boundary conditions: orange points for PBC and black points for OBC. (d), (e) Eigenstates' spatial distribution in the Hermitian and non-Hermitian cases, respectively. Parameters: $m = 2.285 \times 10^{-5}$ of the free electron mass, $\Delta_T = 6$ meV, and $\alpha = 1.7$ meV. For (b) and (d), $\gamma_\pm = 0$; for (c) and (e), $\gamma_+ = 1$ meV, $\gamma_- = 0$.

the value of $\delta\gamma$. The skin modes become more localized when $\delta\gamma$ increases. The enhancement of localization at the right end compensates for the decay of the defect mode resulting in the delocalized behavior. When $\delta\gamma$ is large enough, the NHSE dominates and the ground state becomes localized again Appendix.
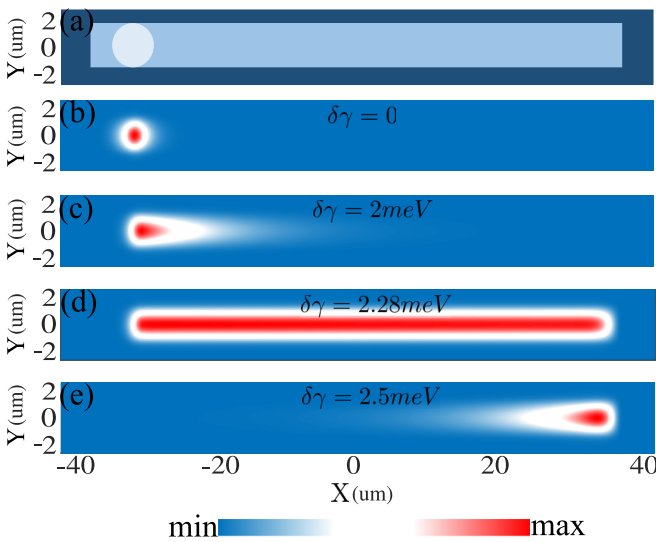

FIG. 2. (a) Schematic figure of a waveguide with a defect on the left-hand side. [(b)–(e)] Spatial distribution of the ground state with different decay rates. Ground state distribution changes drastically from localized inside the defect, dragged into the waveguide, then extended in the waveguide and finally localized at the right end.

IV. LASING IN THE EXTENDED DEFECT MODE

To model polariton lasing, we add to our model phenomenological terms identified previously in the literature as being consistent with experimental observations. These include the gain and nonlinear loss introduced in [68] and energy relaxation factor studied in [69]:

$$i\hbar \frac{\partial \Psi_\pm}{\partial t} = (1 - i\beta)\left[\left(-\frac{\hbar^2 \nabla^2}{2m} + V \mp 2i\alpha \frac{\partial}{\partial x} \right) \Psi_\pm + \Delta_T \Psi_\mp \right] + i(P_\pm - \gamma)\Psi_\pm - i\alpha_1 |\Psi_\pm|^2 \Psi_\pm. \quad (3)$$

Here, β represents energy relaxation, $iP_\pm$ denotes the circular polarized incoherent pump, and α_1 is the nonlinear decay. To achieve the NHSE, we select the incoherent circularly polarized pump to be spatially uniform with different strengths ($P_+ = 3.3$ meV; $P_- = 0$), thus creating different effective decay rates. The steady state is shown in Fig. 3(a), where polaritons are distributed almost uniformly throughout the waveguide. Notice that this distribution is similar to the extended state shown in Fig. 2(d). We then calculate the polariton intensity as a function of energy by Fourier transforming the wave function $\Psi_\pm$ obtained from Eq. (3). Subsequently, we sum up all the intensity along the real space. As shown in Fig. 3(c), the intensity distribution in energy from Fig. 3(a) reveals a peak at around -3.45 meV, which is similar to the extended defect state's eigenenergy calculated by diagonalizing the linear Hamiltonian as shown in Fig. 3(b). This further proves that we have obtained polariton lasing in the extended defect state.
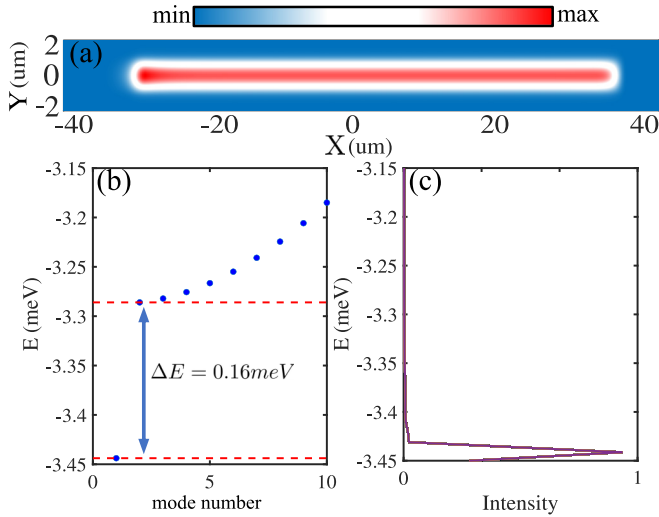
FIG. 3. (a) Steady state's spatial distribution obtained from Eq. (3). The polaritons are uniformly distributed all over the waveguide like the case of Fig. 2(d). (b) Eigenenergies solved in the linear case ($\alpha_1 = 0$). The energy band gap between ground state and others is around 0.16 meV. (c) Intensity of polaritons as a function of energy. Parameters: $\beta = 0.5$, $\alpha = 1.7$ meV, $\Delta_T = 6$ meV, $\alpha_1 = 1\,\mu\text{eV}\,\mu\text{m}^2$, $P_+ = 3.3$ meV, and $P_- = 0$.

V. NONLINEARITY EFFECT ON NHSE AND NON-HERMITIAN MORPHING

Nonlinearity is an intrinsic property of polaritons, so it is an interesting question of whether the NHSE and also the non-Hermitian morphing can persist in the presence of nonlinear interactions. To answer this, we consider the nonlinear interaction term (corresponding to an effective Gross-Pitaevskii equation) by adding $\alpha_2|\Psi_\pm|^2\Psi_\pm$ into the right-hand side of Eq. (3). We first consider a cavity without a defect and show the polaritons are still accumulating at the right end of the system [shown in Fig. 4(a)], which is the signature of the NHSE even with nonlinearity added. Then, we add a defect and show the morphing effect. We find that polaritons can still be distributed all over the cavity, which shows the non-Hermitian morphing is still valid with nonlinearity considered [Fig. 4(b)]. The nonlinear interaction constant is taken to be 1 $\mu\text{eV}\,\mu\text{m}^2$, which is on the same order found in recent experiments [70].
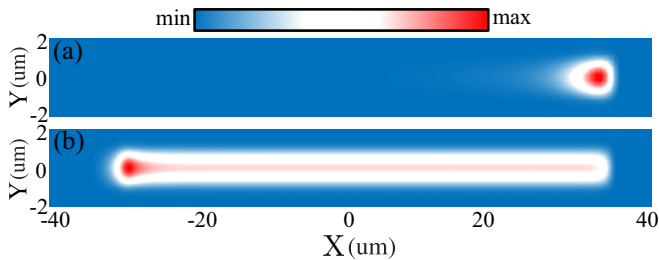

FIG. 4. (a) Polaritons accumulate at the right end of the cavity, which is a signature of NHSE. (b) In the presence of nonlinearity, the ground state can still be extended all over the cavity, which demonstrates the non-Hermitian morphing.

VI. SPATIAL COHERENCE IN AN EXTENDED DEFECT MODE

Owing to the deeper potential, the ground state of the defect carries less energy than the ground state of the waveguide. This energy difference creates a band gap of around 0.2 meV. As a result, after the ground state morphing, it is not only distributed all over the waveguide but is also energetically separated from other modes. This unique property enables the possibility of achieving large-area spatial coherence. We calculate the spatial coherence, $g_1(\Delta x, \Delta y)$ using the formula Appendix

$$g_1(\Delta x, \Delta y) = \frac{\sum_n \Psi_n^*(x, y)\Psi_n(x + \Delta x, y + \Delta y)e^{-\frac{(E_n - E_g)^2}{\delta E^2}}}{\sqrt{I(x, y)I(x + \Delta x, y + \Delta y)}},$$
(4)

$$I(x, y) = \sum_n |\Psi_n(x, y)|^2 e^{-\frac{(E_n - E_g)^2}{\delta E^2}}.$$
(5)

This formula is equivalent to that used in [71], however, assuming a Gaussian energy distribution function. One might have expected a Bose-Einstein distribution; however, it was shown that this results in a poor fit to experiments given the nonequilibrium nature of polariton systems [71]. Here $I(x, y)$ is the intensity profile of polaritons, E_n is the energy of the modes, E_g is the energy of the ground state, and δE is the energy fluctuation. If δE is infinitesimally small corresponding to a perfect condensate, g_1 will equal to 1. In the calculation, we take the reference point (x, y) as the point that has the highest intensity.

In a typical cavity, because of the continuous energy spectrum, more than one mode is excited simultaneously, which results in coherence decay, as shown in Fig. 5(a). It is important to note that, with a larger δE, g_1 drops more rapidly. In comparison, the ground state morphing mode displays better coherence all over the waveguide due to the separation of energy and the extended distribution nature. When δE is small, almost just the ground state is excited and g_1 is nearly one in the whole waveguide. Of course if δE is increased too much, coherence will drop, first at the right end of the waveguide. This can be interpreted as other skin modes being excited, which are dominantly localized at the right edge of the waveguide. Note that the coherence remains high throughout the left region of the waveguide.

A well-known advantage of topological systems is the robustness of their states with respect to disorder (provided that the disorder strength is within the topological band gap). In Figs. 5(c) and 5(d), we compare the spatial coherence in a regular waveguide and our morphing mode system in the presence of disorder (added as a random potential). The morphing scheme retains an enhancement of the spatial coherence length by around 30 times the coherence length of the regular waveguide [72].

To show the usefulness of our proposal, it is important to see whether the spatial coherence can still be preserved in the presence of nonlinear interaction and time-dependent noise. To show this, we consider a Gross-Pitaevskii equation with an additional stochastic term accounting for fluctuations [69,73]. It is based on the truncated Wigner formalism [8,74], keeping the highest order terms in Ψ. The nonlinear term $\alpha_2|\Psi_\pm|^2\Psi_\pm$
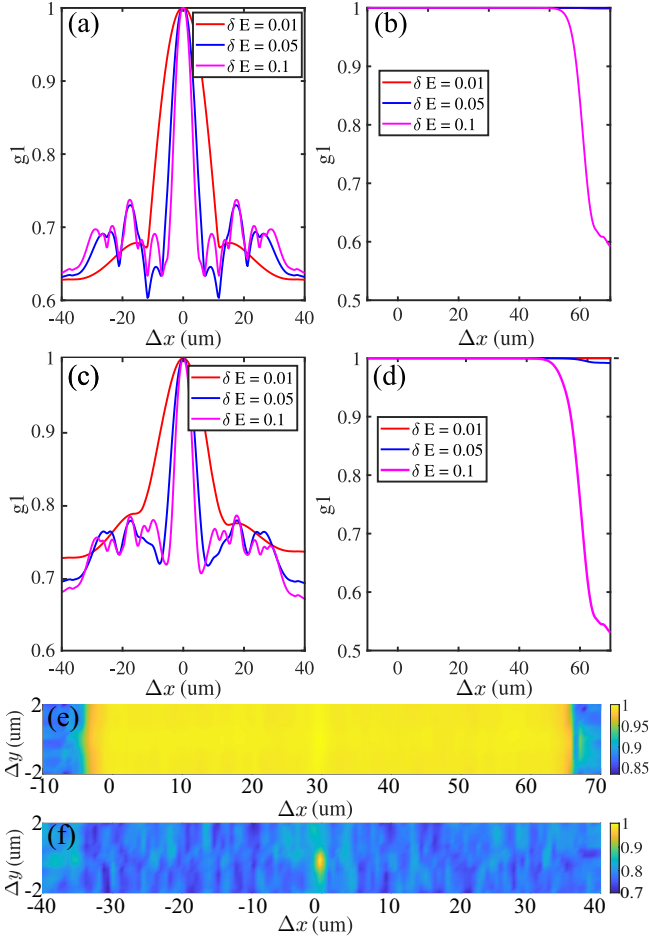
FIG. 5. (a), (b) Spatial coherence calculated from Eqs. (4) and (5) in a normal cavity case and the NHSE morphing case under different strengths of fluctuations, respectively. (c), (d) Spatial coherence calculated in the presence of the same strength of disorder in a normal cavity and the NHSE morphing case. (e), (f) Spatial coherence calculated in the presence of nonlinearity and stochastic noises in the NHSE morphing case and a normal cavity case. Other parameters: $\alpha_2 = 1$ µeV µm^2 [70], $dW_{i,\pm} = \frac{\sqrt{P_\pm + \gamma}}{dx\,dy} \xi_i dt$, where ξ_i is a complex Gaussian noise process satisfying $\langle \xi_i \xi_j^* \rangle = \delta_{ij}/dt$, $\langle \xi_i \xi_j \rangle = 0$, where i, j are discretization indices and $dx(dy)$ is the spacing along the $x(y)$ direction.

and the stochastic term $\frac{dW_\pm}{dt}$ are added into the right hand of Eq. (3). This corresponds to a more explicit treatment of noise in the system and more accurate assessment of coherence. We find that, even with nonlinearity, the coherence can still be enhanced for the topological morphing case.

VII. CONCLUSION

We consider the hybridization of non-Hermitian skin effect modes and a trapped mode in exciton-polariton waveguides. Because of the competition between the trap and NHSE, the localized defect ground state can become extended inside the waveguide. We then show that lasing can be obtained in the extended defect mode. The large band gap of this ground state and the large area distribution properties make it possible to achieve a significant spatial coherence length, considerably

enhanced compared to nontopological systems (more than 30 times). This enhancement survives in the presence of both disorder and nonlinear interactions.

APPENDIX A: DERIVATION OF EQ. (1)

To derive Eq. (1), we start with the Hamiltonian proven in the work [75]. In the first equation of this work, the Hamiltonian is defined:

$$\hat{H} = \frac{\hbar^2 k_x^2}{2m_x} + \frac{\hbar^2 k_y^2}{2m_y} + \hat{H}_{RD} + \frac{1}{2}(E_{X,l} - E_{Y,l'})\hat{\sigma}_x, \quad \text{(A1)}$$

where $\hat{H}_{RD} = -2\alpha\hat{\sigma}_z k_y$ is the Rashba-Dresselhaus Hamiltonian. The Hamiltonian acts on exciton-polaritons, which exist in the plane of a microcavity with coordinates $\vec{x} = (x, y)^T$. We note that polaritons have a two-component spin degree of freedom, corresponding to left and right circularly polarized optical components, written $[\Psi_+(\vec{x}, t), \Psi_-(\vec{x}, t)]^T$. Thus they are represented as a 2-spinor and the above Hamiltonian is of the form of a 2×2 matrix in this basis, where the Pauli matrices are defined as

$$\hat{\sigma}_x = \begin{pmatrix} 0 & 1 \\ 1 & 0 \end{pmatrix}, \quad \hat{\sigma}_z = \begin{pmatrix} 1 & 0 \\ 0 & -1 \end{pmatrix}. \quad \text{(A2)}$$

The wave vectors can be rewritten as operators: $k_x = -i\frac{\partial}{\partial x}$ and $k_y = -i\frac{\partial}{\partial y}$. While in [75], they consider different effective masses m_x and m_y; a simpler case is sufficient for our needs so we will choose $m = m_x = m_y$. Using standard notation, we then use $\frac{\hbar^2}{2m}(k_x^2 + k_y^2) = -\frac{\hbar^2}{2m}(\frac{\partial^2}{\partial x^2} + \frac{\partial^2}{\partial y^2}) = -\frac{\hbar^2}{2m}\nabla^2$. Let us define the constant $\Delta_T = \frac{1}{2}(E_{X,l} - E_{Y,l'})$, which represents a splitting between linearly polarized states at zero wave vector. The Hamiltonian is then

$$\hat{H} = -\frac{\hbar^2\nabla^2}{2m}\begin{pmatrix} 1 & 0 \\ 0 & 1 \end{pmatrix} + 2i\alpha\begin{pmatrix} 1 & 0 \\ 0 & -1 \end{pmatrix}\frac{\partial}{\partial y} + \Delta_T\begin{pmatrix} 0 & 1 \\ 1 & 0 \end{pmatrix}. \quad \text{(A3)}$$

Without loss of generality we can choose a different definition of x and y coordinates to [75], choosing $y \leftrightarrow -x$. Then

$$\hat{H} = -\frac{\hbar^2\nabla^2}{2m}\begin{pmatrix} 1 & 0 \\ 0 & 1 \end{pmatrix} - 2i\alpha\begin{pmatrix} 1 & 0 \\ 0 & -1 \end{pmatrix}\frac{\partial}{\partial x} + \Delta_T\begin{pmatrix} 0 & 1 \\ 1 & 0 \end{pmatrix}$$
$$+ \begin{pmatrix} V(\vec{x}) - i\gamma_+ & 0 \\ 0 & V(\vec{x}) - i\gamma_- \end{pmatrix}. \quad \text{(A4)}$$

We have added to this Hamiltonian a non-Hermitian potential, where the real part is given by $V(\vec{x})$ and taken to be spin independent, while the imaginary part corresponds to spin-dependent but spatially uniform loss in the system.
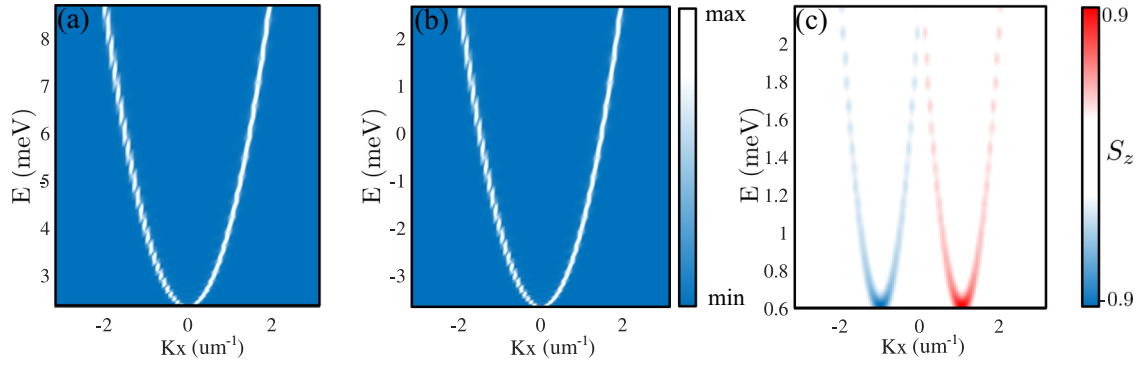
FIG. 6. (a) Band structure obtained from Eq. (1) in the main text without X-Y splitting and RDSOC. (b) Band structure when there is only X-Y splitting (Δ_T) considered. (c) Band structure calculated when there is only RDSOC coupling (α) considered.

We now use the Schrödinger equation to write

$$i\hbar \frac{\partial}{\partial t} \begin{pmatrix} \Psi_+(\vec{x}, t) \\ \Psi_-(\vec{x}, t) \end{pmatrix} = \hat{H} \begin{pmatrix} \Psi_+(\vec{x}, t) \\ \Psi_-(\vec{x}, t) \end{pmatrix} = \begin{pmatrix} \left(-\frac{\hbar^2 \nabla^2}{2m} + V(\vec{x}) - 2i\alpha \frac{\partial}{\partial x} - i\gamma_+\right)\Psi_+(\vec{x}, t) + \Delta_T \Psi_-(\vec{x}, t) \\ \left(-\frac{\hbar^2 \nabla^2}{2m} + V(\vec{x}) + 2i\alpha \frac{\partial}{\partial x} - i\gamma_-\right)\Psi_-(\vec{x}, t) + \Delta_T \Psi_+(\vec{x}, t) \end{pmatrix}. \quad (A5)$$

This corresponds to Eq. (1) of our manuscript and the manipulations used to connect to Eq. (1) of the work in [75].

APPENDIX B: EFFECT OF X-Y SPLITTING AND RDSOC COUPLING

In this section, we investigate the effect of X-Y splitting and RDSOC coupling on the band structure. The band structure is solved from Eq. (1) in the main text. First we calculate the dispersion without X-Y splitting and the RDSOC coupling as shown in Fig. 6(a). Then we turn on the X-Y splitting by choosing $\Delta_T = 6$ meV, $\alpha = 0$ and keep all other parameters the same as in Fig. 1 in the main text. We find that the two spins are still degenerate when there is no RDSOC as shown in Fig. 6(b). Compared to the case without X-Y splitting, the dispersion shift -6 meV, which can be explained by solving the Hamiltonian in reciprocal space:

$$H_{k1} = \begin{pmatrix} \frac{\hbar^2 k^2}{2m} & \Delta_T \\ \Delta_T & \frac{\hbar^2 k^2}{2m} \end{pmatrix}. \quad (B1)$$

We can get two bands with energy $E_1 = \frac{\hbar^2 k^2}{2m} + \Delta_T$, $E_2 = \frac{\hbar^2 k^2}{2m} - \Delta_T$. The dispersions shift ± 6 meV, respectively, and the higher energy band is not within the energy regime calculated here, so only one band is shown in Fig. 6(b).

Then we choose $\Delta_T = 0$ meV, $\alpha = 1.7$ meV and find that two spins are no longer degenerate. Two spins shift towards different directions by $2m\alpha/\hbar^2$ in the reciprocal space. This can be better understood by considering the Hamiltonian in reciprocal space as

$$H_{k2} = \begin{pmatrix} \frac{\hbar^2 k^2}{2m} - 2\alpha k & 0 \\ 0 & \frac{\hbar^2 k^2}{2m} + 2\alpha k \end{pmatrix} \quad (B2)$$

$$= \frac{\hbar^2}{2m} \begin{pmatrix} \left(k - \frac{2m\alpha}{\hbar^2}\right)^2 & 0 \\ 0 & \left(k + \frac{2m\alpha}{\hbar^2}\right)^2 \end{pmatrix} - \frac{2m\alpha^2}{\hbar^2}. \quad (B3)$$

From Eq. (B3) we find that the spin up dispersion shifts towards the positive direction by $2m\alpha/\hbar^2$, while the spin down dispersion shifts in the other direction by the same amount as shown in Fig. 6(c).
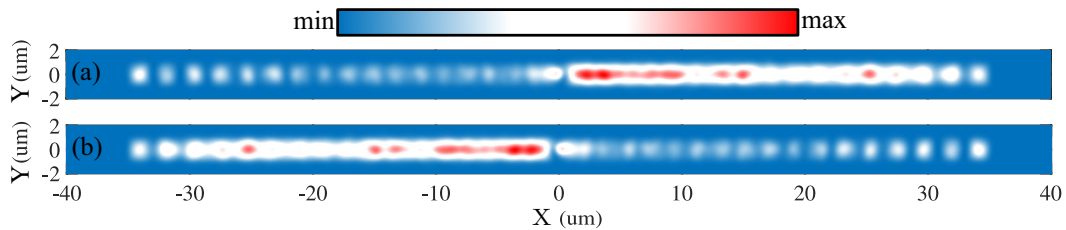

FIG. 7. Polariton time dynamics solved from Eq. (C1) for spin up polaritons (a) and spin down polaritons (b). Spin up and spin down polaritons propagate along opposite directions, which demonstrates the TSHE. Other parameters: $F_\pm = 0$ and $P_\pm = 1$ meV μm^{-1}.
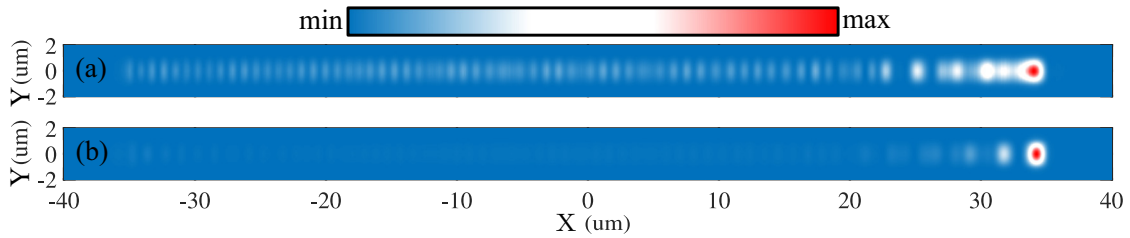
FIG. 8. Polariton time dynamics solved from Eq. (C1) for spin up polaritons (a) and spin down polaritons (b). Both spin up and spin down polaritons propagate along the same direction, which shows the NHSE. Other parameters: $F_+ = 2$ meV, $F_- = 0$, and $P_\pm = 1$ meV μm^{-1}.

APPENDIX C: TIME DYNAMICS FOR TOPOLOGICAL SPIN HALL EFFECT AND NON-HERMITIAN SKIN EFFECT

To illustrate the topological spin Hall effect (TSHE), we choose a linearly polarized coherent pump in the middle of the waveguide. The time dynamics of polaritons is solved from (see Fig. 7)

$$i\hbar \frac{\partial \Psi_\pm}{\partial t} = \left(-\frac{\hbar^2 \nabla^2}{2m} + V \mp 2i\alpha \frac{\partial}{\partial x} + i(F_\pm - \gamma_\pm) \right) \Psi_\pm$$
$$+ \Delta_T \Psi_\mp + P_\pm e^{-i\omega_p t}. \tag{C1}$$

Here $P_\pm$ represents the coherent pump applied in the system and $F_\pm$ corresponds to the incoherent pump. In order to investigate the behavior of TSHE, we set $\gamma_+ = \gamma_- = 0.05$ meV and keep other parameters the same as in Fig. 1. We find that spin up polaritons are propagating towards the right end, while spin down polaritons propagate in the other direction. This corresponds to the signature behavior of the TSHE.

Furthermore, we calculate the time dynamics for polaritons in the non-Hermitian case by applying a spin up polarized incoherent pump, which introduces different effective decay rates. We observe that both spins propagate along the same direction and accumulate at the right end of the waveguide, which shows the NHSE. (See Fig. 8.)

APPENDIX D: ROBUSTNESS OF THE MORPHING EFFECT

To show the robustness of the considered extended ground state, we first introduce a parameter called the inverse participation ratio (IPR), which is used to describe the localization behavior of eigenstates. We divide the system into equally spaced bins, each corresponding to 1 μm in the continuous model to define this quantity:

$$I = \sum_i |\psi_i|^4. \tag{D1}$$

Through definition, I is 1 when the eigenstate accumulates within 1 μm and approaches zero when the eigenstate is extended homogeneously. Given the IPR, we can calculate a

phase diagram corresponding to the dependence of I on Δ_T, $\delta\gamma$ (shown in Fig. 9). We can identify in the diagram different regimes: localized states and delocalized extended states. By looking at the dark blue area, we find that the extended state is not limited to just some specific values but can exist in a region of the parameter space.

APPENDIX E: DERIVATION OF EQ. (4)

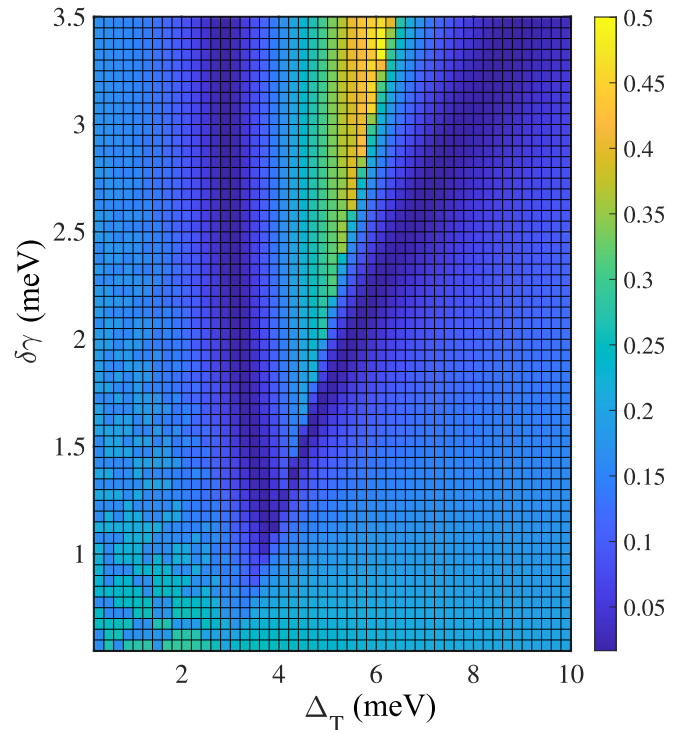Equation (4) can be derived by noting the standard definition of the (first order) spatial coherence [76]:

FIG. 9. Phase diagram for the IPR depending on Δ_T and $\delta\gamma$. The dark blue area corresponds to the extended distribution, while the yellow one corresponds to localized cases.

$$g_1(\Delta x, \Delta y) = \frac{\langle \Psi^*(x, y)\Psi(x + \Delta x, y + \Delta y)\rangle}{\sqrt{\langle \Psi^*(x, y)\Psi(x, y)\rangle \langle \Psi^*(x + \Delta x, y + \Delta y)\Psi(x + \Delta x, y + \Delta y)\rangle}}. \tag{E1}$$

Here the angled brackets denote an ensemble average, which can be recast as a sum over a probability distribution:

$$g_1(\Delta x, \Delta y) = \frac{\sum_n p_n \Psi_n^*(x, y)\Psi_n(x + \Delta x, y + \Delta y)}{\sqrt{\sum_m p_m \Psi_m^*(x, y)\Psi_m(x, y) \sum_l p_l \Psi_l^*(x + \Delta x, y + \Delta y)\Psi_l(x + \Delta x, y + \Delta y)}}. \tag{E2}$$

Here p_n is the probability that the system is in the state Ψ_n. Experiments claiming polariton condensation typically measure an energy distribution peaked about the ground state, E_g. We assume a Gaussian line shape, with width δE, defined by

$$p_n = \frac{1}{N}e^{-(E_n - E_g)^2/\delta E^2}, \tag{E3}$$

where N is a normalization constant. This probability distribution gives Eq. (4).

---

[1] T. D. Visser, *Progress in Optics, Volume 65: A Tribute to Emil Wolf* (Elsevier, Amsterdam, 2020).

[2] D. F. Walls and G. J. Milburn, *Quantum Optics* (Springer, Berlin, 2011).

[3] L. P. Pitaevski and S. Stringari, *Bose-Einstein Condensation* (*Oxford University Press*, Oxford, 2016).

[4] C. W. Wilmsen, H. Temkin, and L. A. Coldren, *Vertical-Cavity Surface-Emitting lasers: Design, Fabrication, Characterization, and Applications* (Cambridge University Press, Cambridge, UK, 2001).

[5] J. Klaers, J. Schmitt, F. Vewinger, and M. Weitz, Nature (London) **468**, 545 (2010).

[6] C. Connaughton, C. Josserand, A. Picozzi, Y. Pomeau, and S. Rica, Phys. Rev. Lett. **95**, 263901 (2005).

[7] A. A. High, J. R. Leonard, A. T. Hammack, M. M. Fogler, L. V. Butov, A. V. Kavokin, K. L. Campman, and A. C. Gossard, Nature (London) **483**, 584 (2012).

[8] I. Carusotto and C. Ciuti, Rev. Mod. Phys. **85**, 299 (2013).

[9] J. Bloch, I. Carusotto, and M. Wouters, Nat. Rev. Phys. **4**, 470 (2022).

[10] P. C. Hohenberg, Phys. Rev. **158**, 383 (1967).

[11] Q. Fontaine, D. Squizzato, F. Baboux, I. Amelio, A. Lemaître, M. Morassi, I. Sagnes, L. Le Gratiet, A. Harouri, M. Wouters, I. Carusotto, A. Amo, M. Richard, A. Minguzzi, L. Canet, S. Ravets, and J. Bloch, Nature (London) **608**, 687 (2022).

[12] L. M. Sieberer, M. Buchhold, and S. Diehl, Rep. Prog. Phys. **79**, 096001 (2016).

[13] D. J. Thouless, M. Kohmoto, M. P. Nightingale, and M. den Nijs, Phys. Rev. Lett. **49**, 405 (1982).

[14] F. D. M. Haldane and S. Raghu, Phys. Rev. Lett. **100**, 013904 (2008).

[15] Z. Wang, Y. D. Chong, J. D. Joannopoulos, and M. Soljačić, Phys. Rev. Lett. **100**, 013905 (2008).

[16] Z. Wang, Y. Chong, J. D. Joannopoulos, and M. Soljačić, Nature (London) **461**, 772 (2009).

[17] P. Zhou, G.-G. Liu, Y. Yang, Y.-H. Hu, S. Ma, H. Xue, Q. Wang, L. Deng, and B. Zhang, Phys. Rev. Lett. **125**, 263603 (2020).

[18] E. Colomés and M. Franz, Phys. Rev. Lett. **120**, 086603 (2018).

[19] W. P. Su, J. R. Schrieffer, and A. J. Heeger, Phys. Rev. B **22**, 2099 (1980).

[20] P. St-Jean, V. Goblot, E. Galopin, A. Lemaître, T. Ozawa, L. Le Gratiet, I. Sagnes, J. Bloch, and A. Amo, Nat. Photon. **11**, 651 (2017).

[21] J. Noh, S. Huang, K. P. Chen, and M. C. Rechtsman, Phys. Rev. Lett. **120**, 063902 (2018).

[22] H. Zhong, Y. Li, D. Song, Y. V. Kartashov, Y. Zhang, Y. Zhang, and Z. Chen, Laser Photon. Rev. **14**, 2000001 (2020).

[23] S. Mittal, V. V. Orre, G. Zhu, M. A. Gorlach, A. Poddubny, and M. Hafezi, Nat. Photon. **13**, 692 (2019).

[24] H.-R. Kim, M.-S. Hwang, D. Smirnova, K.-Y. Jeong, Y. Kivshar, and H.-G. Park, Nat. Commun. **11**, 5758 (2020).

[25] F. Liu and K. Wakabayashi, Phys. Rev. Lett. **118**, 076803 (2017).

[26] S. Mandal, G.-G. Liu, and B. Zhang, ACS Photon. **10**, 147 (2023).

[27] R. Banerjee, S. Mandal, and T. C. H. Liew, Phys. Rev. Lett. **124**, 063901 (2020).

[28] S. Weidemann, M. Kremer, S. Longhi, and A. Szameit, Nature (London) **601**, 354 (2022).

[29] Y. Ao, X. Hu, Y. You, C. Lu, Y. Fu, X. Wang, and Q. Gong, Phys. Rev. Lett. **125**, 013902 (2020).

[30] D. Zou, T. Chen, W. He, J. Bao, C. H. Lee, H. Sun, and X. Zhang, Nat. Commun. **12**, 7201 (2021).

[31] S. Xia, D. Kaltsas, D. Song, I. Komis, J. Xu, A. Szameit, H. Buljan, K. G. Makris, and Z. Chen, Science **372**, 72 (2021).

[32] Q. Yan, B. Zhao, R. Zhou, R. Ma, Q. Lyu, S. Chu, X. Hu, and Q. Gong, Nanophotonics **12**, 2247 (2023).

[33] N. Okuma, K. Kawabata, K. Shiozaki, and M. Sato, Phys. Rev. Lett. **124**, 086801 (2020).

[34] X.-L. Qi, Y.-S. Wu, and S.-C. Zhang, Phys. Rev. B **74**, 045125 (2006).

[35] S. Yao and Z. Wang, Phys. Rev. Lett. **121**, 086803 (2018).

[36] F. Song, S. Yao, and Z. Wang, Phys. Rev. Lett. **123**, 246801 (2019).

[37] W. Zhu, W. X. Teo, L. Li, and J. Gong, Phys. Rev. B **103**, 195414 (2021).

[38] W. Wang, X. Wang, and G. Ma, Nature (London) **608**, 50 (2022).

[39] H. Deng, H. Haug, and Y. Yamamoto, Rev. Mod. Phys. **82**, 1489 (2010).

[40] S. Kim, B. Zhang, Z. Wang, J. Fischer, S. Brodbeck, M. Kamp, C. Schneider, S. Höfling, and H. Deng, Phys. Rev. X **6**, 011026 (2016).

[41] M. Wurdack, E. Estrecho, S. Todd, C. Schneider, A. G. Truscott, and E. A. Ostrovskaya, Phys. Rev. Lett. **129**, 147402 (2022).

[42] D. N. Krizhanovskii, K. G. Lagoudakis, M. Wouters, B. Pietka, R. A. Bradley, K. Guda, D. M. Whittaker, M. S. Skolnick, B. Deveaud-Plédran, M. Richard, R. André, and L. S. Dang, Phys. Rev. B **80**, 045317 (2009).

[43] F. Manni, K. G. Lagoudakis, B. Pietka, L. Fontanesi, M. Wouters, V. Savona, R. André, and B. Deveaud-Plédran, Phys. Rev. Lett. **106**, 176401 (2011).

[44] T. H. Harder, M. Sun, O. A. Egorov, I. Vakulchyk, J. Beierlein, P. Gagel, M. Emmerling, C. Schneider, U. Peschel, I. G. Savenko, S. Klembt, and S. Höfling, ACS Photon. **8**, 1377 (2021).

[45] R. Su, S. Ghosh, T. C. H. Liew, and Q. Xiong, Sci. Adv. **7**, eabf8049 (2021).

[46] P. Kokhanchik, D. Solnyshkov, T. Stöferle, B. Piętka, J. Szczytko, and G. Malpuech, Phys. Rev. Lett. **129**, 246801 (2022).

[47] C.-E. Bardyn, T. Karzig, G. Refael, and T. C. H. Liew, Phys. Rev. B **91**, 161413(R) (2015).

[48] A. V. Nalitov, D. D. Solnyshkov, and G. Malpuech, Phys. Rev. Lett. **114**, 116401 (2015).

[49] S. Klembt, T. H. Harder, O. A. Egorov, K. Winkler, R. Ge, M. A. Bandres, M. Emmerling, L. Worschech, T. C. H. Liew, M. Segev, C. Schneider, and S. Höfling, Nature (London) **562**, 552 (2018).

[50] S. Mandal, R. Ge, and T. C. H. Liew, Phys. Rev. B **99**, 115423 (2019).

[51] R. Bao, S. Mandal, H. Xu, X. Xu, R. Banerjee, and T. C. H. Liew, Phys. Rev. B **106**, 235310 (2022).

[52] R. Banerjee, S. Mandal, and T. C. H. Liew, Phys. Rev. B **103**, L201406 (2021).

[53] T. Gao, E. Estrecho, K. Y. Bliokh, T. C. H. Liew, M. D. Fraser, S. Brodbeck, M. Kamp, C. Schneider, S. Höfling, Y. Yamamoto, F. Nori, Y. S. Kivshar, A. G. Truscott, R. G. Dall, and E. A. Ostrovskaya, Nature (London) **526**, 554 (2015).

[54] W. Gao, X. Li, M. Bamba, and J. Kono, Nat. Photon. **12**, 362 (2018).

[55] R. Su, E. Estrecho, D. Biegańska, Y. Huang, M. Wurdack, M. Pieczarka, A. G. Truscott, T. C. H. Liew, E. A. Ostrovskaya, and Q. Xiong, Sci. Adv. **7**, eabj8905 (2021).

[56] N. H. M. Dang, S. Zanotti, E. Drouard, C. Chevalier, G. Trippé-Allard, M. Amara, E. Deleporte, V. Ardizzone, D. Sanvitto, L. C. Andreani, C. Seassal, D. Gerace, and H. S. Nguyen, Adv. Opt. Mater. **10**, 2102386 (2022).

[57] S. Mandal, R. Banerjee, E. A. Ostrovskaya, and T. C. H. Liew, Phys. Rev. Lett. **125**, 123902 (2020).

[58] S. Mandal, R. Banerjee, and T. C. H. Liew, ACS Photon. **9**, 527 (2022).

[59] H. Xu, K. Dini, X. Xu, R. Banerjee, S. Mandal, and T. C. H. Liew, Phys. Rev. B **104**, 195301 (2021).

[60] X. Xu, H. Xu, S. Mandal, R. Banerjee, S. Ghosh, and T. C. H. Liew, Phys. Rev. B **103**, 235306 (2021).

[61] X. Xu, R. Bao, and T. C. H. Liew, Phys. Rev. B **106**, L201302 (2022).

[62] P. Comaron, V. Shahnazaryan, W. Brzezicki, T. Hyart, and M. Matuszewski, Phys. Rev. Res. **2**, 022051(R) (2020).

[63] M. Król, K. Rechcińska, H. Sigurdsson, P. Oliwa, R. Mazur, P. Morawiak, W. Piecek, P. Kula, P. G. Lagoudakis, M. Matuszewski, W. Bardyszewski, B. Piętka, and J. Szczytko, Phys. Rev. Lett. **127**, 190401 (2021).

[64] Y. Li, X. Ma, X. Zhai, M. Gao, H. Dai, S. Schumacher, and T. Gao, Nat. Commun. **13**, 3785 (2022).

[65] P. Kokhanchik, D. Solnyshkov, and G. Malpuech, Phys. Rev. B **108**, L041403 (2023).

[66] J. Fischer, I. G. Savenko, M. D. Fraser, S. Holzinger, S. Brodbeck, M. Kamp, I. A. Shelykh, C. Schneider, and S. Höfling, Phys. Rev. Lett. **113**, 203902 (2014).

[67] Z. Gong, Y. Ashida, K. Kawabata, K. Takasan, S. Higashikawa, and M. Ueda, Phys. Rev. X **8**, 031079 (2018).

[68] J. Keeling and N. G. Berloff, Phys. Rev. Lett. **100**, 250401 (2008).

[69] E. Estrecho, T. Gao, N. Bobrovska, M. D. Fraser, M. Steger, L. Pfeiffer, K. West, T. C. H. Liew, M. Matuszewski, D. W. Snoke, A. G. Truscott, and E. A. Ostrovskaya, Nat. Commun. **9**, 2944 (2018).

[70] A. Fieramosca, L. Polimeno, V. Ardizzone, L. D. Marco, M. Pugliese, V. Maiorano, M. D. Giorgi, L. Dominici, G. Gigli, D. Gerace, D. Ballarini, and D. Sanvitto, Sci. Adv. **5**, eaav9967 (2019).

[71] O. Tsyplyatyev and D. M. Whittaker, Phys. Status Solidi B **249**, 1692 (2012).

[72] We take a conservative definition of the spatial coherence length as the length over which the first order coherence remains above the level of 99%. For the morphing case, this gives a length of 64 um, while for the regular waveguide it is only 2 um.

[73] M. Wouters, I. Carusotto, and C. Ciuti, Phys. Rev. B **77**, 115340 (2008).

[74] M. Wouters and V. Savona, Phys. Rev. B **79**, 165302 (2009).

[75] K. Rechcińska, M. Król, R. Mazur, P. Morawiak, R. Mirek, K. Łempicka, W. Bardyszewski, M. Matuszewski, P. Kula, W. Piecek, P. G. Lagoudakis, B. Piętka, and J. Szczytko, Science **366**, 727 (2019).

[76] M. O. Scully and M. S. Zubairy, *Quantum Optics* (Cambridge University Press, Cambridge, 1997).